

# On the Occurrence of Portevin–Le Châtelier Instabilities in Ultrafine-Grained 5083 Aluminum Alloys

S.P. Joshi · C. Eberl · B. Cao · K.T. Ramesh ·  
K.J. Hemker

Received: 26 June 2008 / Accepted: 1 December 2008  
© Society for Experimental Mechanics 2009

**Abstract** The Portevin–Le Châtelier (PLC) instability is commonly observed in Al–Mg alloys and is manifested in serrated flow within the stress–strain response. We investigate the persistence of this instability with reduction in grain size by studying an ultrafine-grained (ufg) aluminum alloy (Al5083) and a conventional grain size Al5083. Micro-scale tensile tests combined with digital image correlation (DIC) reveal strength anisotropy and heterogeneity of the deformation in the three material directions (extrusion, rolled, and transverse). For the same applied displacement rate, the PLC effect in ufg-Al5083 is observed only over a small strain range immediately following the yield, while the coarse-grained Al5083 exhibits serrated flow over nearly the entire plastic strain range. These observations are explained using the stability analysis of Hähner (Acta Mater 45:3695–3707, 1997), and implications for nanocrystalline (nc) alloys are discussed.

**Keywords** Portevin–Le Châtelier instability · Grain size · Micro-tensile testing · DIC · Stability analysis

## Introduction

Aluminum alloys have been candidates as structural materials owing to their impressive specific strength (yield strength/density). Recently, the strength of these materials has been significantly improved by the process of grain size refinement. Al-alloys with sub-micron grain sizes are produced by a variety of processing methods that involve severe plastic deformations (SPD) such as extrusion, torsion, or cryomilling [1, 2]. Al5083 alloy (Al–5 Mg) is particularly popular as a structural material because of its superior weldability, corrosion resistance and impact resistance [3]. Furthermore, ultrafine-grained (ufg) Al5083 alloys with grain size ( $d$ )  $\sim 100$  nm–1  $\mu$ m have shown impressive strengths when used as the matrix material for particulate composites [4]. However, SPD processed ufg materials typically suffer from limited strain hardening capacity [5, 6], which results in susceptibility to deformation instabilities due to the lack of stabilizing mechanisms. One instability that is commonly observed even in some coarse-grained ( $d \gg 1$   $\mu$ m) Al–Mg alloys is the Portevin–Le Châtelier (PLC) instability in the post-yield region at quasi-static rates of loading ( $10^{-5}$ – $10^{-2}$  s $^{-1}$ ) [7]. In a displacement controlled uniaxial tension experiment, the PLC behavior manifests in serrated flow (stress drops) and is attributed to the interaction of dislocations with solute atoms through the phenomenon known as dynamic strain aging (DSA). The DSA causes spatially inhomogeneous plastic flow over a range of applied strain [8, 9].

It is of interest to investigate the implications of this mechanism of instability in nc and ufg materials, especially in

---

S.P. Joshi (✉)  
Department of Mechanical Engineering,  
National University of Singapore,  
Singapore 117576, Singapore  
e-mail: shailendra@nus.edu.sg

S.P. Joshi · C. Eberl · B. Cao · K.T. Ramesh (SEM member) ·  
K.J. Hemker  
Department of Mechanical Engineering,  
The Johns Hopkins University,  
Baltimore, MD 21218, USA

C. Eberl  
Institut für Zuverlässigkeit von Bauteilen und Systemen,  
Universität Karlsruhe,  
Kaiserstr. 12,  
76131 Karlsruhe, Germany



the wake of depleted stabilizing mechanisms. Although there is rich literature available on PLC behavior in different materials (see for example [10–14]), the effects of microstructure arising from the grain size have not been investigated thoroughly [7, 11, 15]. In this paper, we investigate the persistence of this instability with reduction in grain size by studying an ufg aluminum alloy (Al5083) and a conventional grain size Al5083 (cg-Al5083) combining micro-scale tensile testing with *in-situ* imaging for digital image correlation (DIC) based analysis. Micro-tensile tests are particularly suitable for ufg materials, which are generally available only in small quantities. The *in-situ* imaging technique allows a visual approach to tracking the PLC bands during the test, and DIC technique provides high fidelity in calculating multi-axial strain fields that are often spatially and temporally inhomogeneous [16–18]. In the next section we briefly describe the experimental set up and image correlation technique. In subsequent sections, we discuss the experimental results on ufg-Al5083 and cg-Al5083, and the anisotropy in the PLC behavior of ufg-Al5083 as related to the underlying microstructures. Finally, we briefly discuss the experimental observations from a theoretical viewpoint using the stability analysis of Hähner [10].

## Experimental Technique and Results

### Materials and Methods

#### *Specimen preparation*

The ufg-Al5083 provided by Prof. E. J. Lavernia (University of California, Davis) was made by cryomilling Al5083 powder, followed by consolidation using hot isostatic pressing (HIPping) and extrusion, and then rolling in to a plate. Figure 1 reveals the anisotropy of the microstructure of the as-received material seen from the transmission electron microscopy (TEM). The grains in the extrusion direction are elongated with a typical aspect ratio of about 2:1. The microstructure in the rolled direction shows only small evidence of elongated grains. From the transverse microstructures we estimate an average grain size ( $d$ ) of about 400–450 nm. Slices 1 mm thick are cut from this bulk sample using a wire electro discharge machining (EDM) technique. A dog-bone shaped graphite electrode is used to punch out micro-samples by a sink EDM process through the thickness from each slice, for tension experiments along the extrusion (ED), rolled (RD, along the rolling direction) and transverse (TD, in the rolling plane but perpendicular to the rolling direction) directions [defined in Fig. 2(a)]. The specimen gage length and width are about 1.7 mm (overall length~3 mm) and 500  $\mu\text{m}$ , respectively. The punched out samples were ground to a

thickness of 250  $\mu\text{m}$  and the faces of the specimen were carefully polished to obtain a surface roughness of less than 1  $\mu\text{m}$ . The resulting surface roughness can be used to track deformation of the specimen during the test by digital image correlation. The final specimen thicknesses range from 130–200  $\mu\text{m}$ .

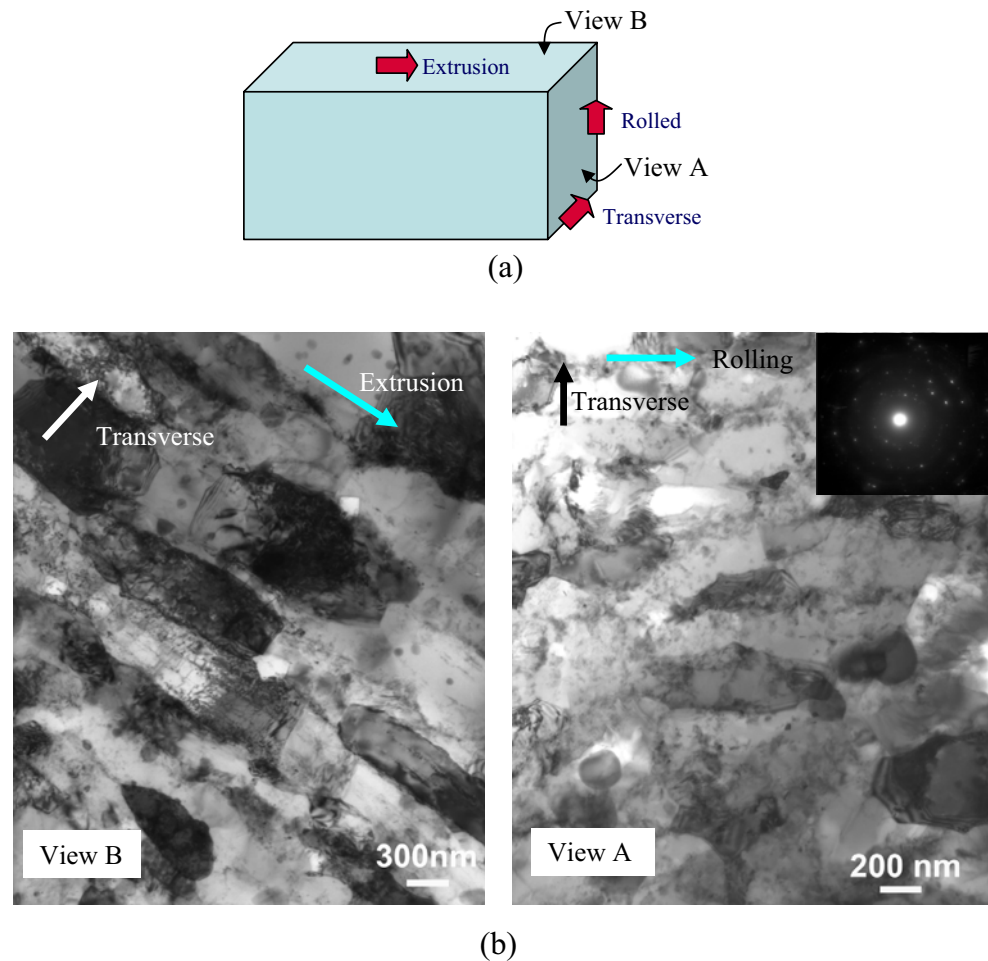
#### *Test setup and analysis (digital image correlation)*

The custom-built micro tensile setup [Fig. 2(b)] is equipped with an actuator, a 20 lb load cell with a noise level of about 0.1 N (which translates to a stress of about 1.5 MPa for our micro-tensile specimens), an air bearing and a digital camera (Pixelink, PL-782) used at a frame rate of 1 image per second (approximately 500–1,500 images were captured and analyzed per test). The lens attached to the camera allows a field of view [FOV, Fig. 2(c)] of roughly  $3 \times 2 \text{ mm}^2$  giving a resolution of 1 pixel/ $\mu\text{m}$ . The setup is controlled by a Matlab (Mathworks®, [www.Mathworks.com](http://www.Mathworks.com)) based graphical user interface which also controls the data acquisition. The custom-built setup allows triggering the camera and can perform controlled tensile tests, strain rate jump tests and creep tests. The digital image correlation (DIC) and tracking code was developed in-house at the Johns Hopkins University and utilizes Matlab© and can be freely downloaded from the Mathworks website (<http://www.mathworks.com/matlabcentral/fileexchange/loadFile.do?objectId=12413&objectType=File>). The DIC code analyzes an image series taken during the test to extract the displacement fields [19]. The DIC suite also contains a tool to analyze these displacement fields to characterize global and local displacement and strain. The images captured during the experiments were analyzed with a subset size of  $20 \times 20$  or  $30 \times 30$  square-pixels. The size of the subset determines the fidelity of the calculated displacements. Larger subsets tend to smoothen out the displacement calculation but also reduce the displacement resolution in the two specimen directions (axial and transverse) as each subset now identifies a larger area than what a smaller subset would represent. As a result, these subsets may overlap giving inaccurate measure of strain.

#### *Measurement procedure*

The typical procedure starts with the alignment of the sample grips to guarantee uniaxial load conditions. The sample is positioned in the grips, a small pre-load is applied to allow the sample to settle in the grips and then the sample get fixed using superglue and the sample grips are tightened. Typically the superglue is cured in an hour and the optical system can be set up. After the test the sample with grips is removed from the setup and the superglue dissolved in acetone.

**Fig. 1** (a) Directions associated with ufg-Al5083: Extrusion (ED), Rolled (RD) and Transverse (TD), and (b) TEM images of cryomilled, HIPped, rolled and extruded Al5083 (ufg-Al5083). The inset in *View A* shows the diffraction pattern in the transverse direction



The average global strain can be calculated by a linear regression of the displacement calculated from the DIC analysis. Note that a careful selection of the grid size and spacing is required to account for inhomogeneities. In our tests, the gage length ( $L$ ), defined by the grid length, is kept the same to allow a consistent comparison of the ductility of the specimens in different directions.

The formation of shear bands in the material under investigation leads to an inhomogeneous deformation behavior. For the measurement of local strains analyzed in this paper, a fine displacement field was analyzed by DIC to be able to resolve the strain in the shear bands.

## Results

### Yield strength

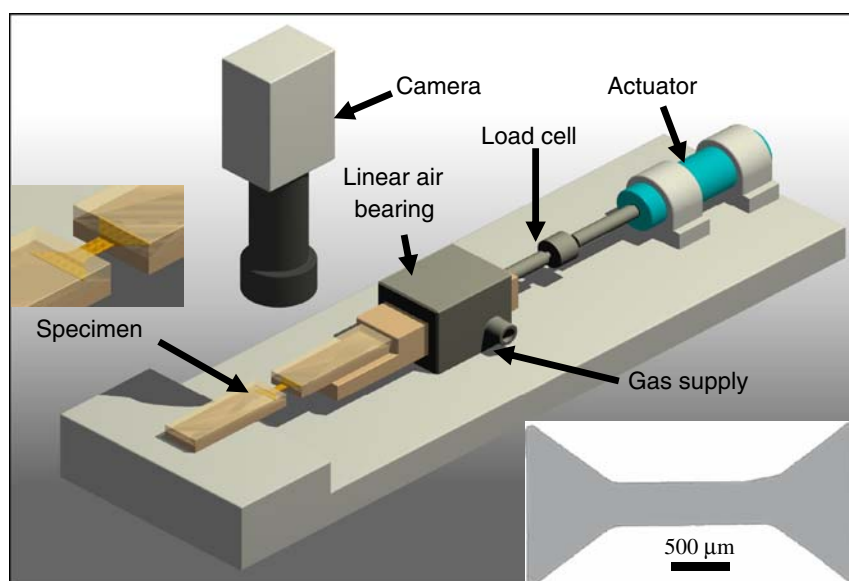
Uniaxial tension tests were performed on the ED, RD and TD specimens (i.e., specimens oriented for tension along the ED, RD and TD axes) at nominal strain rates of  $3.0 \times 10^{-5}$ – $5.0 \times 10^{-5} \text{ s}^{-1}$ . Figure 3 shows the true stress–true strain response for the ufg-Al5083 in the three material directions. The true strain in the figure is defined here as the

average strain measured as the slope of the linear fit to the  $u$ – $L$  plot obtained from the DIC procedure at time  $t$ , where  $u$  is the average axial displacement over the gage length  $L$  ( $=1,530 \text{ }\mu\text{m}$ ) of the grid marked [see Fig. 3 inset for a qualitative representation of grid]. Figure 3 also shows the results from a micro-tension test conducted on coarse-grained Al5083-H131 (cg-Al5083) with grain size in the range of tens of microns. We note that the two materials have been produced through different processing routes the cg-Al5083 was made from an ingot while the ufg-Al5083 was processed via powder metallurgy. The behavior of cg-Al5083 has been well-documented in the literature, e.g. [20]. As is expected, the ufg-Al5083 is stronger than the cg-Al5083, primarily because of the grain size strengthening.

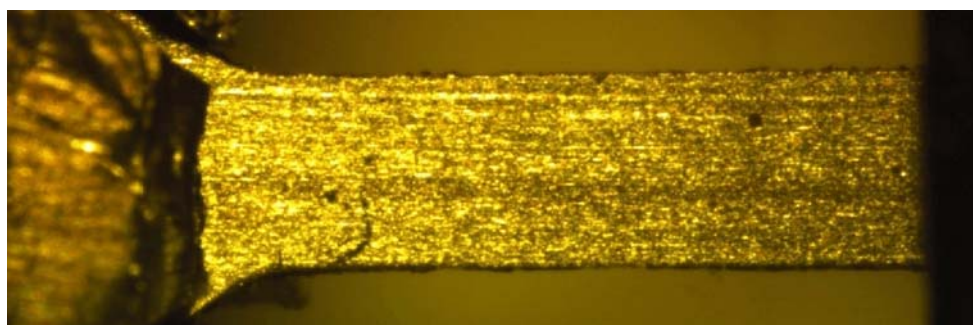
### Post-yield behavior

The ufg-Al5083 shows anisotropic deformation behavior in the three directions (ED, RD, and TD). The TD possesses the lowest strength, and also has the lowest failure strain (Table 1). Note that the ufg-Al5083 shows failure strains that are comparable (except in the TD) to the cg-Al5083 despite the lower strain hardening. The post-yield responses

**Fig. 2** (a) Schematic of micro-tension test setup consisting of an actuator, a load cell, a linear air bearing and a digital camera. [Bottom right inset: Typical Al5083 micro-tension specimen], and (b) field of view (FOV) for the Pixelink (PL-782) camera lens is about  $3 \times 2 \text{ mm}^2$



(a)



(b)

of both ufg-Al5083 and cg-Al5083 show a serrated behavior (stress drops) on the stress-strain curves (with some important differences, discussed next). Each drop in the stress correlates with the occurrence of a narrow band in the specimen. This behavior, referred to as the Portevin–Le Châtelier (PLC) effect, is commonly observed in Al–Mg alloys. The occurrence of PLC effect is a strain-rate softening instability primarily attributed to the phenomenon of dynamic strain aging (DSA) caused by the dislocation–solute interactions. A detailed description of different types of PLC bands can be obtained from [7]. Based on this classification, the observed PLC behavior in the ED specimen are categorized as type-A instability in that a band appears to initially nucleate near the shoulder region of the micro-tensile coupon followed by multiple continuously propagating bands.

There are some important differences in the observed serrated flow responses of the ufg and cg-Al5083. First, the flow serrations in ufg-Al5083 commence almost immediately following yield; in contrast, there exists an *incubation* strain or critical strain ( $\epsilon_c$ ) for the cg-Al5083 before the serrated flow sets in. Second, the frequency of serrations is

much smaller in ufg-Al5083 compared to cg-Al5083. Third, the strain range over which serrated flow occurs is narrow for ufg-Al5083, whereas for the cg-Al5083 serrations occur over the entire plastic flow regime beyond  $\epsilon_c$ . In other words, there is an upper strain limit ( $\epsilon'_c$ ) for the PLC instability in this ufg-Al5083. This observation has not been reported in the literature for ufg-Al5083. However, few experimental observations of this upper strain limit have been reported for other materials with much coarser grain sizes. We discuss these differences our results within a theoretical context later in the paper.

The chemical composition (Table 2) shows the presence of a high amount of oxygen in ufg-Al5083 compared to cg-Al5083. Our STEM (Scanning TEM) analysis [Fig. 5(a)] indicates that Mg is inhomogeneously distributed and preferentially located at the grain boundaries (gb) as indicated by the light contrast in Fig. 5(b). The presence of Mg at gb's has also been reported in other nc and ufg Al–Mg materials [1, 21]. The corresponding depletion of Mg in solid solution may contribute to the diminished serrated flow in the ufg-material. It is interesting to note



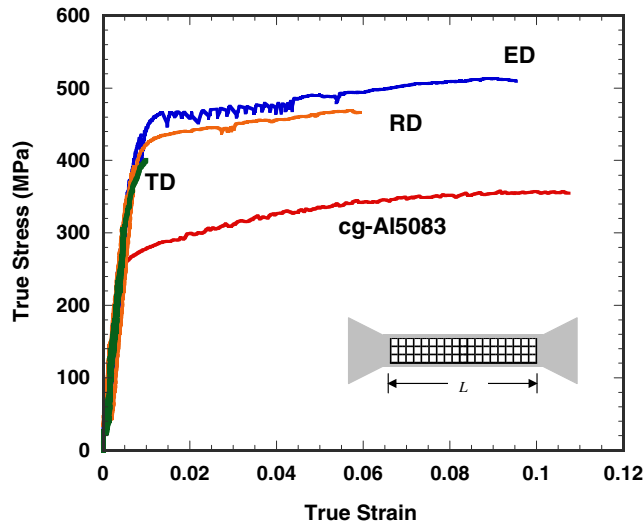


**Fig. 3** True stress–true strain curves for ufg and cg-Al5083

that the oxygen is also preferentially located at the gb's [Fig. 5(c)]. We note that a similar STEM analysis on cg-Al5083 focusing near a gb region [Fig. 5(d)] does not indicate segregation of Mg near the gb [Fig. 5(e)].

The serrated flow behavior was found to be different in different directions for the ufg-Al5083. This can be seen in the ED and RD curves in Fig. 3. The TD does not exhibit any global ductility; hence no serrated flow could be recorded at the macroscale. For the same nominal strain rate, the serrated behavior for three different ED specimens involved larger serrations on the macroscale than that for three RD specimens (Fig. 4) and it occurred over a larger strain range. Even when the serrations in the overall stress–strain curves are small (as in the RD specimens), the PLC instability can be observed using the local DIC analysis.

Although the DSA mechanism is expected to be active irrespective of the directionality of the specimen (with respect to the underlying microstructure), the anisotropy of grain size and shape in rolled materials have been shown to affect the intensity of stress drops in Al–Mg alloys [12]. For ufg-Al5083, we occasionally observe larger stress drops in ED than in RD (Fig. 4); similar observations have been reported on mechanically alloyed as well as cryomilled Al–Mg alloys [1]. Brindley and Worthington [11] observed that the magnitude of the stress drop decreases with increasing grain size in Al–3%Mg alloy. However, the grains appear to be more elongated in the ED than in the

**Table 1** Tensile properties of ufg-Al5083

Direction	0.2% proof strength (MPa)	Ultimate strength (MPa)	Failure strain (%)
Extrusion	410	510	10.0
Rolled	395	470	7.0
Transverse	330	355	1.05

**Table 2** Chemical composition of ufg-Al5083 and cg-Al5083

	ufg-Al5083	cg-Al5083
Oxygen	0.41	–
Nitrogen	0.26	–
Silicon	0.12	0.40
Iron	0.25	0.40
Copper	0.08	0.10
Manganese	0.62	0.40–1.0
Magnesium	4.57	4.0–4.9
Chromium	0.076	0.05–0.25
Zinc	0.008	0.25
Titanium	0.017	0.15
Other	<0.15	0.15
Aluminum	Remainder	Remainder

other two directions (Fig. 1). Our results and those of Witkin and Lavernia [1] are in contrast to the observations of Brindley and Worthington [11] on Al–Mg alloys. Note that Diazdon [15] showed the reverse trend in nickel. The dependence of the magnitude of the stress drop on grain size thus remains uncertain. However, we note that there are two related issues: grain size and mobile dislocation density. UFG materials made by SPD have both smaller grains and higher initial dislocation density. The grain sizes in the studies of [11, 12] were at least one order of magnitude larger than our ufg-Al5083. Given that the ufg-Al5083 has undergone severe plastic deformation (during cryomilling and consolidation processes) it is reasonable to assume that the initial dislocation density is high; however, the mobile dislocation density may be low given the small grain size, and most dislocations may act as forests, reducing the DSA activity and possibly causing limited serrated flow in the ufg-Al5083.

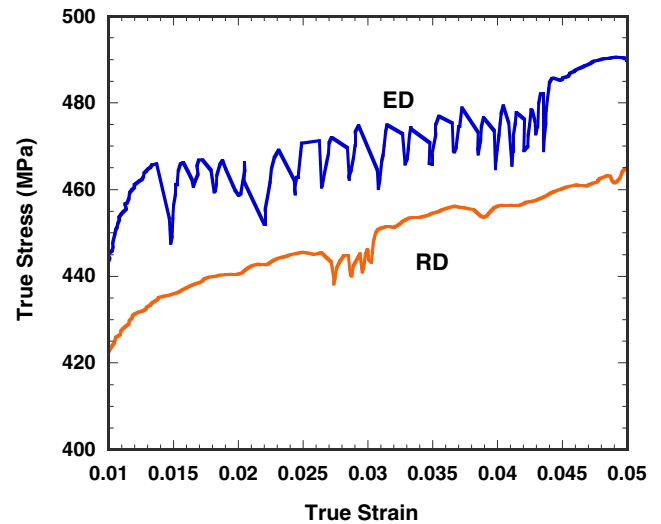
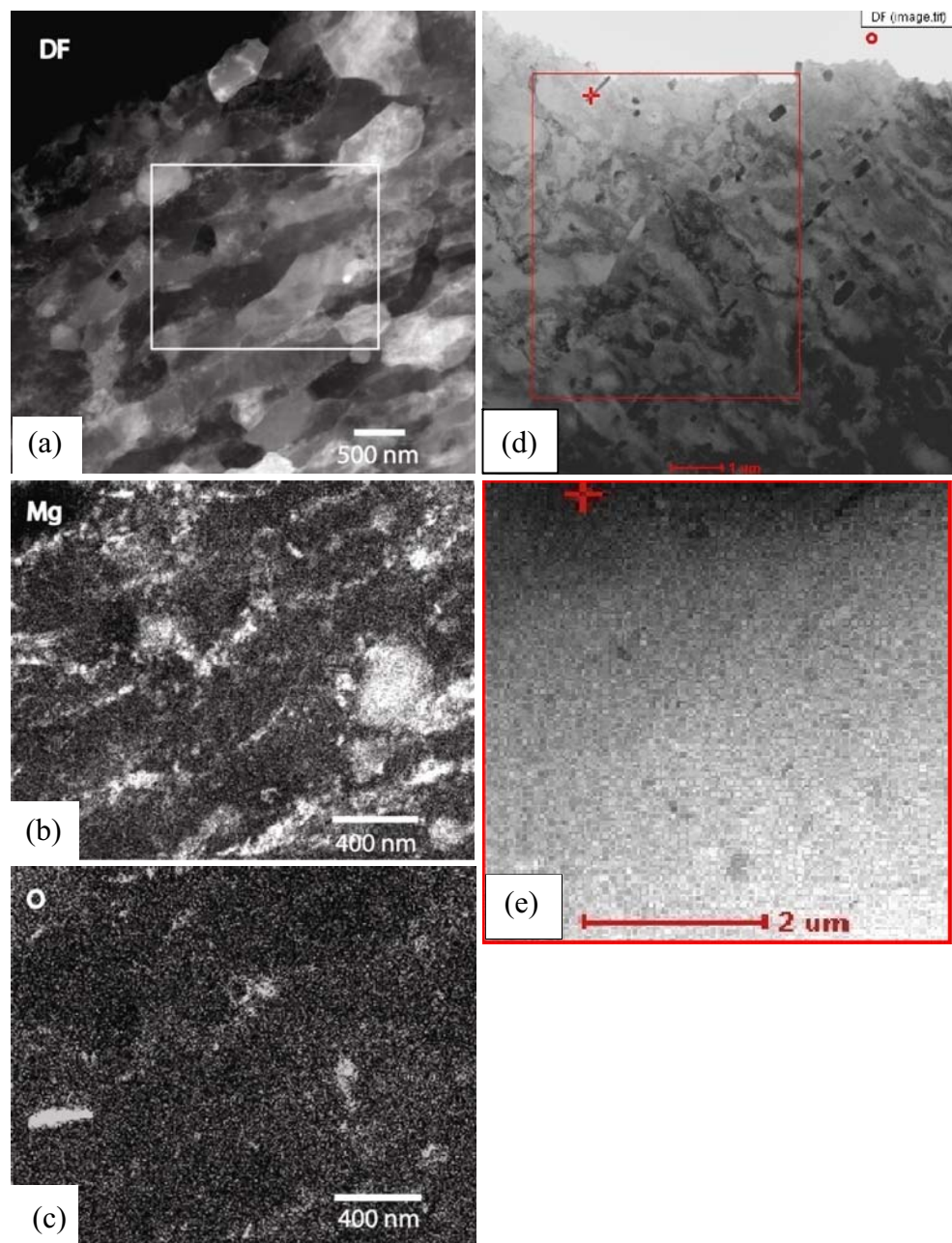


**Fig. 4** Enlarged view of the differences in the serrated flow in ED and RD for ufg-Al5083. The unusual stress drops are related to the lower image acquisition rate. The inset shows the load versus time behavior captured with a higher sample rate for the ED direction

**Fig. 5** (a) Dark field (DF) TEM image [View B, Fig 1(b)]; STEM maps of (b) magnesium, and (c) oxygen in the boxed region of (a). (d) Dark field (DF) TEM image of a GB region in CG-Al5083; (e) STEM map of magnesium in the boxed region of (d)



#### PLC band characteristics in ufg-Al5083

The DIC technique is particularly advantageous in characterizing the PLC instability in the ufg-Al5083. We describe the band characteristics for one ED specimen in some depth. For this specimen the serrated behavior is easily discernable both from the stress-strain curve (Fig. 4) and the images. We analyze different regions of the ED specimen along its gage length to quantify the heterogeneity of strain distribution during the occurrence of a PLC band. Each stress drop corresponds to occurrence of a narrow band in the specimen. For the particular case of the ED serrated behavior (Fig. 4) a discrete band occurs at a new location. Figure 6(a) is the load-time plot for the ED

specimen. Figures 6(b–g) show the temporal evolution of the axial strain and the occurrence of PLC bands that coincide with the conspicuous load drops in Fig. 6(a); note that the bands are oriented approximately  $\pm 45^\circ$  to the axial direction indicating a shear instability. The width of a PLC band for this 150  $\mu\text{m}$  thick specimen is about 110  $\mu\text{m}$ , which is comparable to the specimen thickness. Note the development of conjugate bands as time progresses, propagation of the banded region across the specimen, and the development of large axial strain in that region.

Figure 7(a) shows the overall plot of the axial strain versus time for the ED responses in Figs. 4 and 5. For the purpose of explaining this result, we discretize the gage length ( $L = 1,530 \mu\text{m}$ ) into six bins; no. 1 being the leftmost

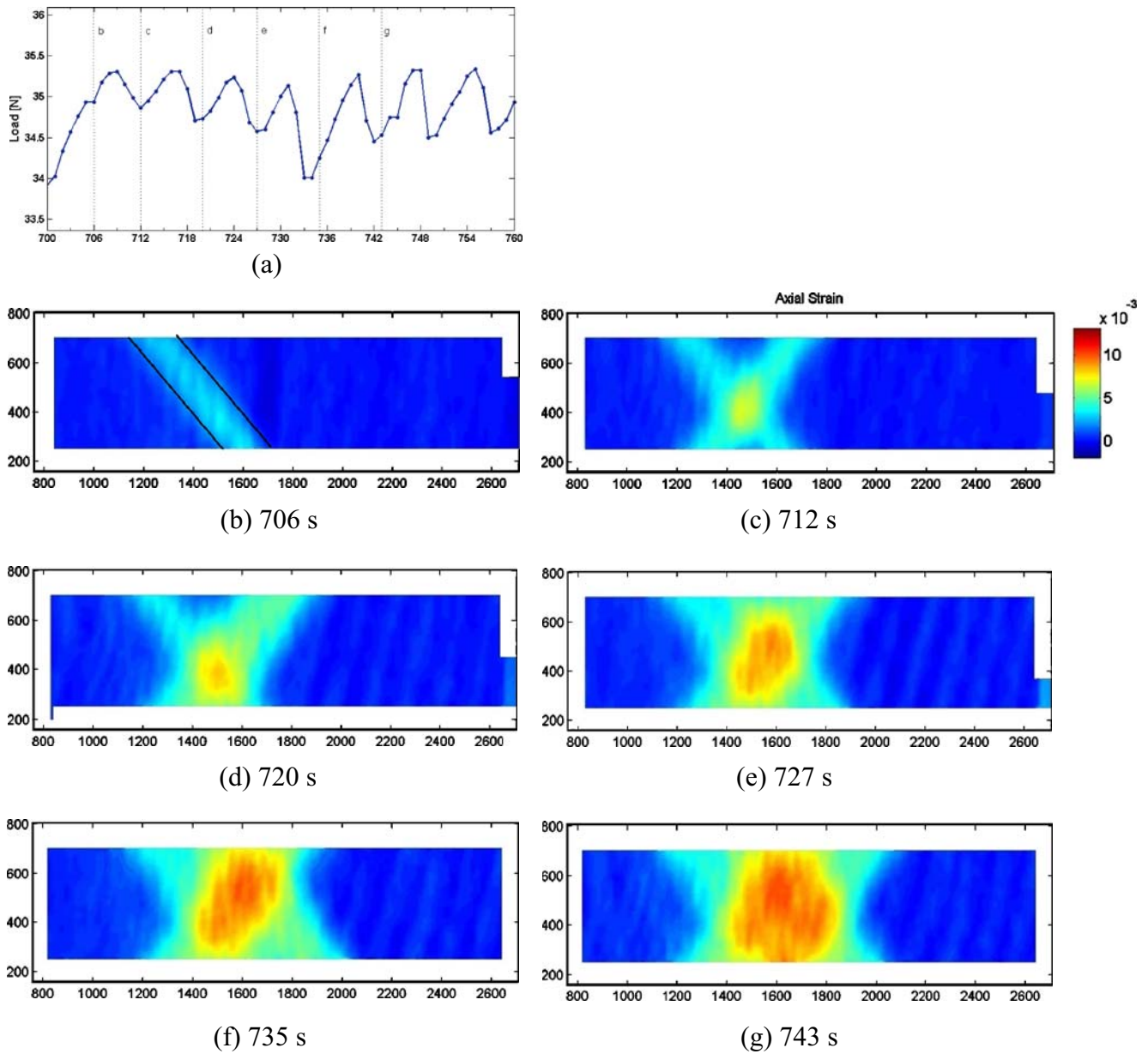


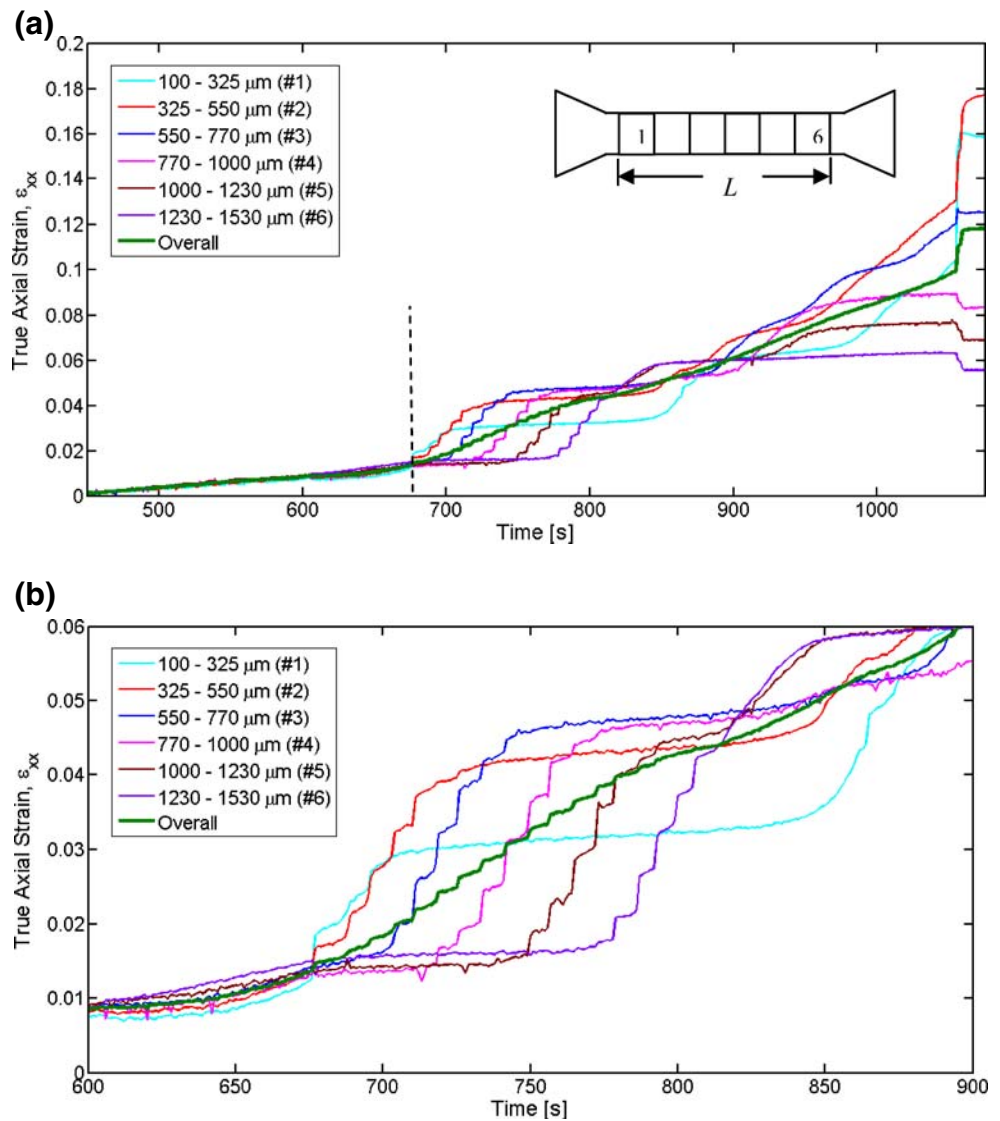
**Fig. 6** (a) Enlarged view showing the load drops for the ED specimen (ref. Fig. 4), (b–g) indicate the evolution of strain in the ED specimen corresponding to the times shown in (a) (the abscissa and ordinates indicated in pixels). In (b), the localized strain indicates a PLC band. The width of this band (demarcated by solid lines) is about  $110\ \mu\text{m}$  (measured from pixels)

bin, and so forth. The six curves correspond to the strain evolution as a function of time in each of these bins. To begin with, the deformation rate is homogeneous up to about 1.5% strain indicated by the vertical dashed line) as evident from the fact that all the six curves overlay. This is followed by the first occurrence of the strain localization event (PLC instability), characterized by a sudden jump in the strain of about 1.5% (the cyan curve, no. 1) that occurs over a time-scale of approximately 45 s (giving a nominal rate  $\sim 3.33 \times 10^{-4}\ \text{s}^{-1}$  in that region). However, this jump is not a single strain burst. Rather, we observe three smaller jumps within this big jump that corroborate with the

occurrence of multiple bands in this region oriented at  $45^\circ$  to the horizontal axis. Thus, the band thickness estimated in Fig. 5(a) ( $\sim 706\ \text{s}$ ) is likely a combination of thinner bands that are in close proximity. Eventually, the strain in this region saturates at about 3.0%. It is interesting to note that while the strain is increasing in no. 1 the strain in the neighboring region (no. 2) has already begun to evolve [Fig. 7(b)]. Note that the bin size ( $\sim 220\text{--}230\ \mu\text{m}$ ) is larger than the typical band width [ $\sim 110\ \mu\text{m}$ , Fig. 6(a)]; therefore, it is possible that the simultaneous evolutions in no. 1 and no. 2 are two independent bands, although it could also be an indication of one shear band that cuts across the



**Fig. 7** (a) Strain evolution for ED ufg-Al5083 specimen, (b) enlarged view of the PLC events, (c) spatial variation of the axial strain along the center of the specimen at  $t=706$  s [Fig. 6(b)]. The strain is measured in the center of the specimen to be able to measure the shear band width, and (d) temporal evolution of strain in the localized region at the point of maximum strain (marked *A*) in (c)



specimen at an angle and gets recorded in multiple bins (see below).

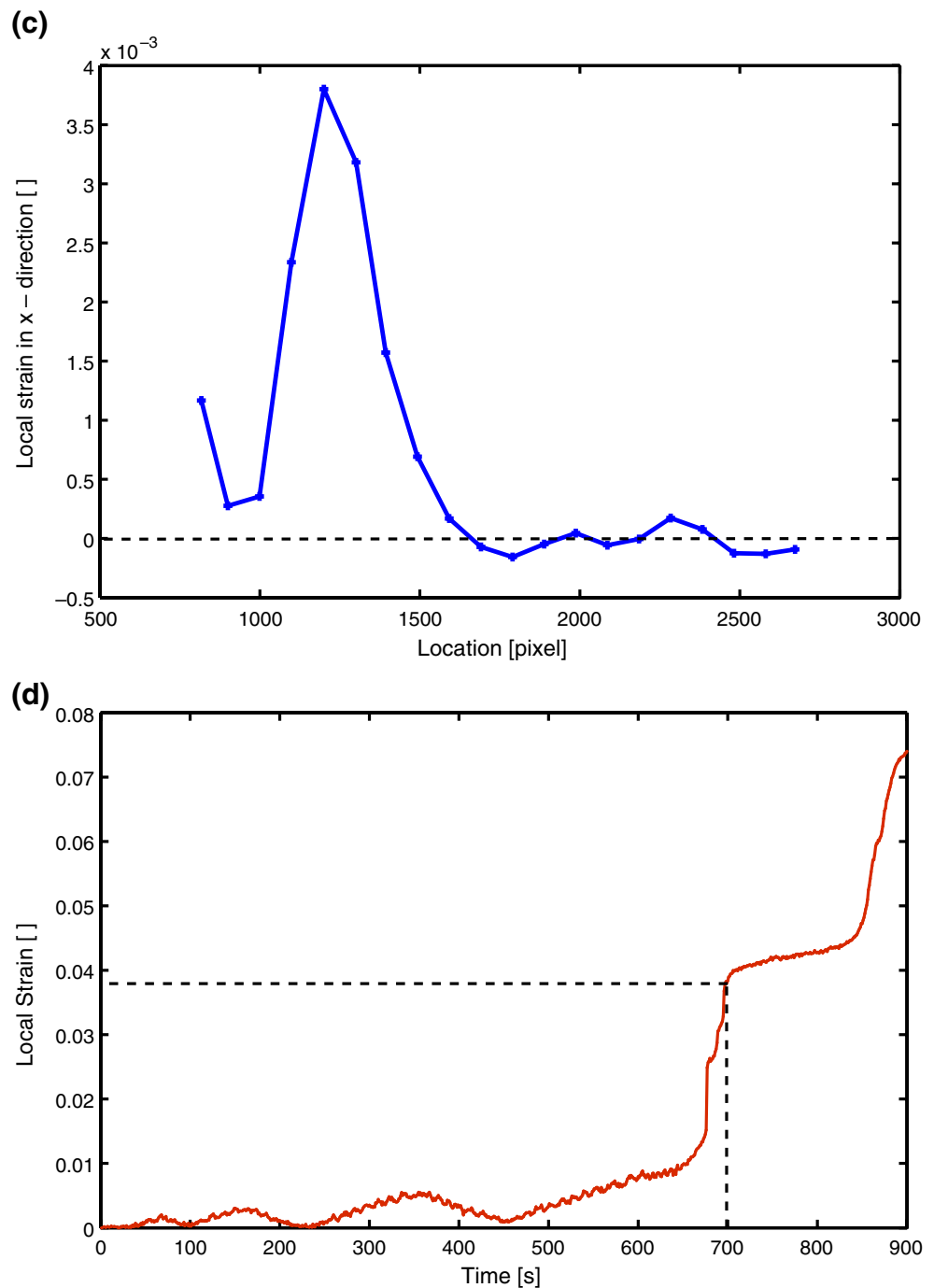
For example, in the former situation, the reason for strain saturation in no. 1 is possibly due to the immediately adjacent region (no. 2) beginning to soften independently as a result of the PLC effect in this region. The maximum strain is higher in no. 2; however, the evolution process is very similar to that of no. 1. Subsequently, the strain in no. 2 saturates to about 4%. As observed from Fig. 7(b), the neighboring region (no. 3) has already invoked the PLC response (giving a strain jump of  $\sim 2.5\%$  over 75 s). This trend of deferred strain evolution and saturation may indicate a *spatial coupling* of strain [22] and minimizes the possibility of a single event causing a runaway instability. Figure 7(c) indicates the spatial variation of the axial strain along the specimen center at  $t=706$  s [corresponding to Fig. 6(b)], while Fig. 7(d) indicates the temporal evolution of the maximum axial strain in Fig. 7(c).

We note however, that as more and more bands evolve, a newly developed band might share two bins. This may lead to a spatial aliasing, an artifact due to the specific approach adopted here in the method of plotting, which can be mistaken as the inherent material behavior of spatial coupling. Inclined grids or bins can minimize the spatial aliasing, but it cannot be avoided because typically the bands observed are conjugate bands.

As the inhomogeneous deformation spreads over the gage length the overall strain reaches a higher value ( $\sim 6\%$ ); at later stages the inhomogeneous deformations are still persistent but less discrete. Finally, the strain localizes in one region (no. 2 in this case) and the specimen fails at  $45^\circ$  to the axial direction. As seen from the figure, the overall strain is about 12% (green solid curve) but locally (no. 2) the ductility is higher (18% strain). The observed overall ductility for ufg-Al5083 despite low hardening (compared to cg-Al5083)



Fig. 7 (continued)



in ED and RD (Fig. 3) may be attributed to this *diffuse* nature of instability in an ufg material that would otherwise be highly susceptible to localization.

### Theoretical Considerations

Kubin and Estrin [14] developed some of the key ideas to model instability regimes in materials exhibiting DSA. Elaborate nonlinear dynamics [23] and numerical [24, 25]

analyses have been performed to reveal the spatio-temporal coupling in the PLC behavior as a function of applied strain rate. The effect of microstructure is emphasized in these analyses. However, it is difficult to generalize these approaches to address a range of materials, because the PLC behavior is a strong function of microstructure and chemical composition, which depend on material processing. On the other hand, linear stability analyses [9, 26, 27] can provide simple yet useful qualitative trends as a function of the microstructural

processes (e.g. hardening, slip modes etc.). We discuss the qualitative differences in the PLC behavior of ultra-fine-grained and coarse-grained-Al5083 with reference to the differences in their underlying microstructure using the stability analysis of Hähner [10].

### Strain Regime of Serrated Flow

The plastic flow is assumed to occur through a thermally activated dislocation glide process [28] defined by

$$\dot{\varepsilon} = \nu \Omega \exp \left[ -\frac{G_0 + \Delta G}{kT} + \frac{\sigma_{\text{eff}} V}{kT} \right] \quad (1)$$

where  $\nu$  is the Debye frequency,  $G_0$  is the constant activation enthalpy in the absence of DSA,  $\Delta G$  is the maximum increase of the free activation enthalpy due to DSA,  $\sigma_{\text{eff}}$  is the effective stress (defined et seq.), and  $V$  is the activation volume. The elementary or unit strain  $\Omega$  is defined by  $\Omega = \rho_m b / \sqrt{\rho_f}$ , where  $\rho_m$  is the mobile dislocation density,  $\rho_f$  is the forest dislocation density, and  $b$  is the magnitude of the Burgers vector. Solving equation (1) for  $\sigma_{\text{eff}}$ , we obtain

$$\sigma_{\text{eff}} = S_0 \left( \ln \left( \frac{\dot{\varepsilon}}{\nu \Omega} \right) + \left( \frac{G_0 + \Delta G}{kT} \right) \right), \quad (2)$$

where  $S_0 = \frac{kT}{V}$ . The parameter  $S_0$  is sometimes called the strain rate sensitivity (SRS) parameter and has the dimensions of stress. The effective stress  $\sigma_{\text{eff}}$  driving the thermally activated process is defined as

$$\sigma_{\text{eff}} = \sigma_{\text{ext}} - [f(\varepsilon) + \sigma_0] \quad (3)$$

where  $\sigma_{\text{ext}}$  is the external applied stress,  $f(\varepsilon)$  includes the contributions from hardening due to accumulated plastic strain ( $\varepsilon$ ) and prior plastic work (e.g. cryomilling, extrusion, and rolling in ufg-Al5083), and  $\sigma_0 = \sigma_f + k_y d^{-1/2}$  includes the friction stress ( $\sigma_f$ ) and the strengthening due to the grain size. From equations (2) and (3), and assuming linear hardening  $f(\varepsilon) = h\varepsilon$ , we have

$$\sigma_{\text{ext}} = \underbrace{S_0 \left( \ln \left( \frac{\dot{\varepsilon}}{\nu \Omega} \right) + \left( \frac{G_0 + \Delta G}{kT} \right) \right)}_{\sigma_{\text{eff}}} + \underbrace{(h\varepsilon + H + \sigma_f + k_y d^{-1/2})}_{\sigma_{\text{int}}} \quad (4)$$

where  $h$  is the hardening modulus ( $= \partial \sigma_{\text{ext}} / \partial \varepsilon|_{\dot{\varepsilon}}$ ),  $H$  is the hardening from prior plastic work,  $k_y$  is the Hall–Petch coefficient (at constant strain), and  $d$  is the mean grain size. Equation (4) relates the applied stress to the rate of plastic deformation and the intrinsic strengths derived from the microstructure (including grain size effects). In comparison, there is a characteristic rate—which we shall call  $\eta$ -associated with the dynamic strain aging, and which arises

from the mobility of the solute atoms that diffuse through the material. The interaction of these two rates determines the domain over which dynamic strain aging is observed in a material.

Hähner [10] defines a non-dimensional effective strain hardening parameter  $B$ , derived from a stability analysis, that in our case is given by

$$B = \frac{(h - \sigma_{\text{ext}}) V \Omega}{kT} - \frac{V \Omega^2 h}{kT \Omega'} (1 + \Omega \Omega' \varepsilon), \quad (5a)$$

where  $\Omega' = \partial \Omega / \partial \varepsilon$ . The usefulness of  $B$  is provided by the stability analysis: instability sets in when the parameter  $B$  falls below a critical value  $B_c$ . The two competing rates can be used to define (Hähner [10]) a scaled timelike variable  $X^* = \frac{\eta \Omega}{\dot{\varepsilon}}$ , the evolution of which (with strain) is given by  $X = X^* + \frac{\eta \Omega'}{\dot{\varepsilon}} \varepsilon$ , and the strain hardening can be scaled by the evolution of  $\Omega$  with strain through  $m = \frac{V \Omega^2 h}{kT \Omega'}$ . The strain hardening parameter  $B$  of equation (5a) can be then rewritten in terms of these scaled variables as

$$B = \underbrace{\frac{(h - \sigma_{\text{ext}}) V \Omega}{kT}}_{B^*} - \underbrace{\frac{m}{X^*} (X - X^*)}_{B_1} \quad (5b)$$

The effective hardening behavior of the material with evolving strain can then be represented in terms of the variation of  $B$  with the scaled variable  $X$ , as shown in Fig. 8. This behavior is of course only sensible after yield, and the onset of yield represents a jump to the point  $(B^*, X^*)$  in the  $(B, X)$  space—this initial point is of course dependent on material behavior (e.g.,  $B^*$  will be larger for coarse grained Al5083 than for ultra-fine-grained Al5083, because of the low  $h$  and the grain size strengthening in the latter material). Subsequent deformation results in movement along a path with negative slope of magnitude  $(m/X^*)$ , and again this slope will be different for the two materials considered here, being larger for the coarse-grained case (because of higher  $h$ ). Using the explicit grain size dependence introduced into equation (5b) by  $\sigma_0 = k_y d^{-1/2}$  (the Hall–Petch component) and neglecting  $\sigma_f$  from equation (4) gives us

$$B = \underbrace{\frac{h \Omega V}{kT} - \frac{k_y \Omega V}{kT} \left( \frac{1}{d^{1/2}} \right)}_{B^*} - \underbrace{\frac{m (X - X^*)}{\Omega' X^*}}_{B_1}. \quad (6)$$

The two triangular  $(B-X)$  trajectories in Fig. 8 correspond schematically to the response of the two different materials [equations (5b) and (6)], shown in blue (coarse-grained Al 5083) and orange (ultra-fine-grained Al 5083). The rising parts (the dotted straight lines) of the trajectories are identical, and represent the loading portion that is

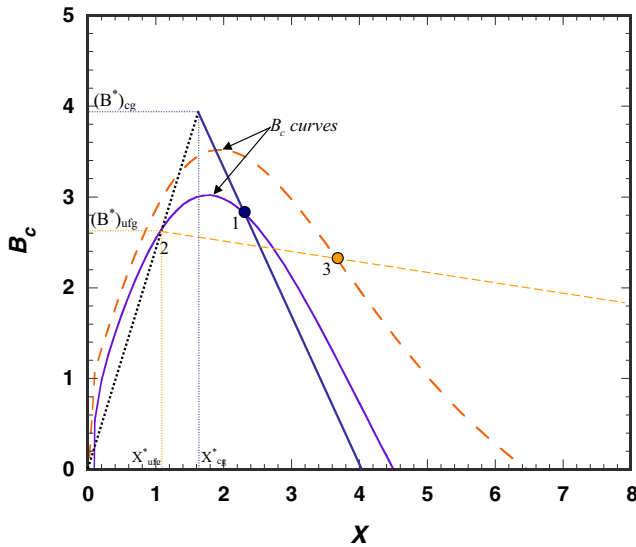


**Fig. 8** (Color online) Schematic representations of critical strain regimes for the serrated flow behavior in ufg (dashed orange) and cg (solid blue) materials

proportional to the applied rate. The yield condition corresponding to the apex of the triangle, point  $(B^*, X^*)$ , is different for the two materials, being higher in  $B^*$  for the coarse-grained material. The falling parts (the solid and dashed straight lines) represent the  $\frac{m}{X^*}(X - X^*)$  term in equation (5b), and are again different for the two materials, falling more steeply for the coarse-grained material (because of the higher  $h$ ).

Hähner [10] shows that the instability will occur when  $B$  is less than a certain critical value  $B_c$ , which is itself an evolving function of strain and is given by

$$B_c = (1 + X^3) \left( e^{-X} - \frac{Y}{X} \right), \quad (7)$$

where  $Y = kT/\Delta G$  is a strain aging parameter. Equation (7) depends strongly on  $Y$ , which is itself a function of microstructure through  $\Delta G$ . In terms of the evolving strain, this means that the instability will occur whenever a curve representing  $B(X)$  [represented by equation (5b)] lies below a curve representing  $B_c(X)$  [represented by equation (7)]. We also show qualitative examples of such  $B_c(X)$  curves in Fig. 8. For a typical coarse-grained material such as our cg-Al5083, a curve such as the solid blue curve is expected (where we have chosen  $Y=0.05$  because the low  $\rho_f$  implies low  $\Delta G$ ). For a typical ultra-fine-grained material such as our ufg-Al5083, we expect a curve such as the dashed orange curve in Fig. 8, because the plastic work leads to higher  $\rho_f$  which implies high  $\Delta G$  and therefore lower  $Y$ .

Application of the instability condition to Fig. 8 then indicates that in the cg-Al5083 the serrated flow should have a delayed occurrence after the yield (i.e. an incubation strain will exist for the serrated flow, corresponding to point

1 in Fig. 8 and referred to as  $\varepsilon_c$  in the “Results” section), following which serrated flow should continue until failure. This is what is observed. For the ufg-Al5083, Fig. 8 demonstrates that the onset of instability should occur immediately on yield (because  $B^*$  is within the  $B_c(X)$  curve for the ufg material): this corresponds to point 2 in Fig. 8. The system becomes stable again at point 3 in Fig. 8, when  $B^* > B_c$ , which represents a termination strain (referred to as  $\varepsilon'_c$  in the “Results” section). Thus one would expect the serrated flow to begin immediately following the yield and terminate after some time for the ufg material, and this is what is observed.

This qualitative illustration compares the serrated flow behaviors of the ufg and cg-Al5083 with reference to the activation energy barrier ( $\Delta G$ ), hardening ( $h$ ) and grain size ( $d$ ). We speculate on implications for general ufg and nc materials in the following. Many SPD processed nc materials exhibit non-linear strain hardening: a high hardening over a small range of strain (<1%) followed by a weak hardening. This is attributed to initially high dislocation density development followed by its rapid saturation. Further, the large volume fractions of grain boundaries may act as sinks for dislocations, resulting in depleted strain hardening. Correspondingly, the decreasing part of the  $B(X)$  trajectory [the second term in equation (5b)] may be non linear, and this may have implications on the incubation and termination strains. Further, the activation energy  $\Delta G$  may also be influenced by the grain size, and the changes in activation volumes ( $V$ ) with grain size and crystal structure [29] will also play a role in determining the PLC behavior for a given material. Thus, the overall PLC response in ufg and nc materials (such as the aluminum alloy in this case) is strongly tied to the crystal structure and deformation mechanisms in the material, in addition to the processing routes that determine the underlying microstructure.

## Summary

We investigate the persistence of the PLC instability in ufg-Al5083 with reduction in grain size by comparing it with a cg-Al5083 alloy. DIC-enabled micro-scale tensile tests reveal the heterogeneity of the deformation in the three material directions. The characteristics of the PLC response in the cryomilled ufg-Al5083 are attributed to the processing conditions that lead to high strength and low hardening, which result in early occurrence of the termination strain in comparison to the cg-Al5083 as explained through the stability analysis of Hähner [10]. The analysis indicates that the PLC response is intimately tied to not only the grain size but also the processing route adopted to achieve it. Therefore, a detailed assessment of the PLC response of the

grain size effect should involve a rigorous experimental scheme of alloys with a nominally same grain size, but produced from different processes, for example, via SPD and electro-deposition routes.

**Acknowledgements** The authors would like to thank Prof. E.J. Lavernia for providing the material samples and for the TEM images of ufg-A15083. SPJ, BC and KTR acknowledge the financial support received from the Army Research Laboratory (W911NF-06-2-0006). CE and KJH acknowledge the financial support received from AFOSR under the MEANS-2 Program (Grant No. FA9550-05-1-0173).

## References

- Witkin DB, Lavernia EJ (2006) Synthesis and mechanical behavior of nanostructured materials via cryomilling. *Prog Mater Sci* 51:1–60. doi:10.1016/j.pmatsci.2005.04.004
- Valiev RZ, Islamgaliev RK, Alexandrov IV (2000) Bulk nanostructured materials from severe plastic deformation. *Prog Mater Sci* 45:103–189. doi:10.1016/S0079-6425(99)00007-9
- Newbery AP, Nutt SR, Lavernia EJ (2006) Multi-scale al 5083 for military vehicles with improved performance. *JOM* 58:56–61. doi:10.1007/s11837-006-0216-4
- Ye J, Han BQ, Lee Z, Ahn B, Nutt SR, Schoenung JM (2005) A tri-modal aluminum based composite with super-high strength. *Scr Mater* 53:481–486. doi:10.1016/j.scriptamat.2005.05.004
- Meyers MA, Mishra A, Benson DJ (2006) Mechanical properties of nanocrystalline materials. *Prog Mater Sci* 51:427–556. doi:10.1016/j.pmatsci.2005.08.003
- Wang YM, Ma E (2004) Three strategies to achieve uniform tensile deformation in a nanostructured metal. *Acta Mater* 52:1699. doi:10.1016/j.actamat.2003.12.022
- Robinson JM, Shaw MP (1994) Microstructural and mechanical influences on dynamic strain aging phenomena. *Int Mater Rev* 39:113–122
- Zaiser M, Hähner P (1997) A unified description of strain-rate softening instabilities. *Mater Sci Eng A* 238:399. doi:10.1016/S0921-5093(97)00468-1
- Zaiser M, Haehner P (1997) Oscillatory modes of plastic deformation: theoretical concepts. *Physica Status Solidi (B). Basin Res* 199:267–330
- Hähner P (1997) On the critical conditions of the Portevin–Le-Chatelier effect. *Acta Mater* 45:3695–3707. doi:10.1016/S1359-6454(97)00066-9
- Brindley BJ, Worthington PJ (1969) Serrated yielding in aluminum-3% magnesium. *Acta Metall* 17:1357–1361. doi:10.1016/0001-6160(69)90153-9
- Cheng X-M, Morris JG (2000) The anisotropy of the portevin-le chatelier effect in aluminum alloys. *Scr Mater* 43:651–658. doi:10.1016/S1359-6462(00)00474-7
- Jiang H, Zhang Q, Chen X, Chen Z, Jiang Z, Wu X, Fan J (2007) Three types of portevin-le chatelier effects: experiment and modelling. *Acta Mater* 55:2219. doi:10.1016/j.actamat.2006.10.029
- Kubin LP, Estrin Y (1990) Evolution of dislocation densities and the critical conditions for the portevin-le chatelier effect. *Acta Metall Mater* 38:697–708. doi:10.1016/0956-7151(90)90021-8
- Dziadon A (1996) The effect of grain size on serrated flow in nickel. *Scr Mater* 34:375–380. doi:10.1016/S0956-716X(95)00537-6
- Bouabdallah K, Balland P, Tabourot L, Vacher P (2007) Contribution of kinematic field measurements to the modelling of the portevin-le cha?Telier effect by the image correlation method. *J Strain Anal Eng Des* 42:589–594. doi:10.1243/03093247JSA312
- Tong W, Tao H, Zhang N, Hector LG Jr (2005) Time-resolved strain mapping measurements of individual portevin-le chatelier deformation bands. *Scr Mater* 53:87–92. doi:10.1016/j.scriptamat.2005.03.020
- Besnard G, Hild F, Roux S (2006) “Finite-element” displacement fields analysis from digital images: application to Portevin–Le Chatelier bands. *Exp Mech* 46:789–803. doi:10.1007/s11340-006-9824-8
- Chu TC, Ranson WF, Sutton MA (1985) Applications of digital-image-correlation techniques to experimental mechanics. *Exp Mech* 25:232. doi:10.1007/BF02325092
- Park KT, Park JH, Lee YS, Nam WJ (2005) Microstructures developed by compressive deformation of coarse grained and ultrafine grained 5083 al alloys at 77 k and 298 k. *Mater Sci Eng A* 408:102–109. doi:10.1016/j.msea.2005.07.040
- Soer WA, De Hosson JTM, Minor AM, Morris JW Jr, Stach EA (2004) Effects of solute mg on grain boundary and dislocation dynamics during nanoindentation of al-mg thin films. *Acta Mater* 52:5783–5790. doi:10.1016/j.actamat.2004.08.032
- Lebyodkin M, Dunin-Barkowskii L, Bréchet Y, Estrin Y, Kubin LP (2000) Spatio-temporal dynamics of the portevin-le chatelier effect: experiment and modelling. *Acta Mater* 48:2529–2541. doi:10.1016/S1359-6454(00)00067-7
- Bharathi MS, Rajesh S, Ananthakrishna G (2003) A dynamical model for the portevin-le chatelier bands. *Scr Mater* 48:1355. doi:10.1016/S1359-6462(02)00653-X
- Kok S, Beaudoin AJ, Tortorelli DA, Lebyodkin M, Kubin L, Fressengeas C (2003) Simulation of the portevin-le chatelier effect using polycrystal plasticity. *J Phys IV: JP* 105:191. doi:10.1051/jp4:20030187
- Kok S, Bharathi MS, Beaudoin AJ, Fressengeas C, Ananthakrishna G, Kubin LP, Lebyodkin M (2003) Spatial coupling in jerky flow using polycrystal plasticity. *Acta Mater* 51:3651–3662. doi:10.1016/S1359-6454(03)00114-9
- Mesarovic S (1995) Dynamic strain aging and plastic instabilities. *J Mech Phys Solids* 43:671–700. doi:10.1016/0022-5096(95)00010-G
- Yang SY, Tong W (2006) A perturbation analysis of the unstable plastic flow pattern evolution in an aluminum alloy. *Int J Solids Struct* 43:5931. doi:10.1016/j.ijsolstr.2005.07.041
- Rizzi E, Haehner P (2004) On the portevin-le chatelier effect: theoretical modeling and numerical results. *Int J Plast* 20:121–165. doi:10.1016/S0749-6419(03)00035-4
- Wei Q, Cheng S, Ramesh KT, Ma E (2004) Effect of nanocrystalline and ultrafine grain sizes on the strain rate sensitivity and activation volume: Fcc versus bcc metals. *Mater Sci Eng A* 381:71. doi:10.1016/j.msea.2004.03.064